A Dense Block Model Representing Western Continental United States Deformation for the 2023 Update to the National Seismic Hazard Model

Eileen L. Evans*[1]

Abstract

Seismic hazard assessment, such as the U.S. Geological Survey (USGS) National Seismic Hazard Model (NSHM), relies on estimates of fault slip rate based on geology and/or geodetic observations such as the Global Navigation Satellite System (GNSS), including the Global Positioning System. Geodetic fault slip rates may be estimated within a 3D spherical block model, in which the crust is divided into microplates bounded by mapped faults; fault slip rates are determined by the relative rotations of adjacent microplates. Uncertainty in selecting appropriate block-bounding faults and in forming closed microplates has limited the interpretability of block models for seismic hazard modeling. By introducing an automated block closure algorithm and regularizing the resulting densely spaced block model with total variation regularization, I develop the densest and most complete block model of the western continental United States to date. The model includes 853 blocks bounded by 1017 geologically identified fault sections from the USGS NSHM Fault Sections database. Microplate rotations and fault slip rates are constrained by 4979 GNSS velocities and 1243 geologic slip rates. I identify a regularized solution that fits the GNSS velocity field with a root mean square misfit of 1.9 mm/yr and reproduces 57% of geologic slip rates within reported geologic uncertainty and model sensitivity, consistent with other geodetic-based models in this Focus Section. This block model includes slip on faults that are not included in the USGS NSHM Fault sections database (but are required to form closed blocks) for an estimate of "off-fault" deformation of 3.62×10^{19} N·m/yr, 56% of the total calculated moment accumulation rate in the model.

Cite this article as Evans, E. L. (2022). A Dense Block Model Representing Western Continental United States Deformation for the 2023 Update to the National Seismic Hazard Model, *Seismol. Res. Lett.* **93**, 3024–3036, doi: 10.1785/0220220141.

Supplemental Material

Introduction

Understanding the geometric complexity of the Pacific–North America plate motion is necessary for understanding North American tectonics (e.g., Thatcher *et al.*, 2016) and for quantitative seismic hazard (e.g., Petersen *et al.*, 2014). The plate boundary is partitioned across a complex fault network that extends over 1000 km inland, including the San Andreas fault system in California, the Juan de Fuca plate and subduction zone in the Pacific northwest, and a broad range of extension characterized by low-slip-rate normal faults in the Basin and Range province (Fig. 1).

Revealing the kinematics of a complex plate boundary zone requires integrating continental scale (>1000 km) and regional scale (<1000 km) microplate and fault system geometries. Quantifying crustal deformation across faults typically relies on estimates of the fault slip rate, the rate at which displacement on a fault occurs on tectonic time scales (e.g., Savage and Burford, 1973). Satellite geodetic observations such as Global Navigation Satellite Systems (GNSS) including the Global Positioning System (GPS) and Interferometric Synthetic Aperture Radar (InSAR) record active contemporary accumulation of tectonic strain across seismogenic fault zones over years to decades. Estimates of the fault slip rate from geodesy (geodetic slip rates) must be calculated in a fault model in which fault geometry and properties are prescribed and modeled (e.g., Evans, 2018). Alternatively, estimates of the fault slip rate can be made directly at points along a fault using tectonic geomorphology or paleoseismology (geologic slip rates, e.g., Wallace, 1968). Geologic techniques are capable of probing

1. Department of Geological Sciences, California State University, Northridge, California, U.S.A.

*Corresponding author: eileen.evans@csun.edu

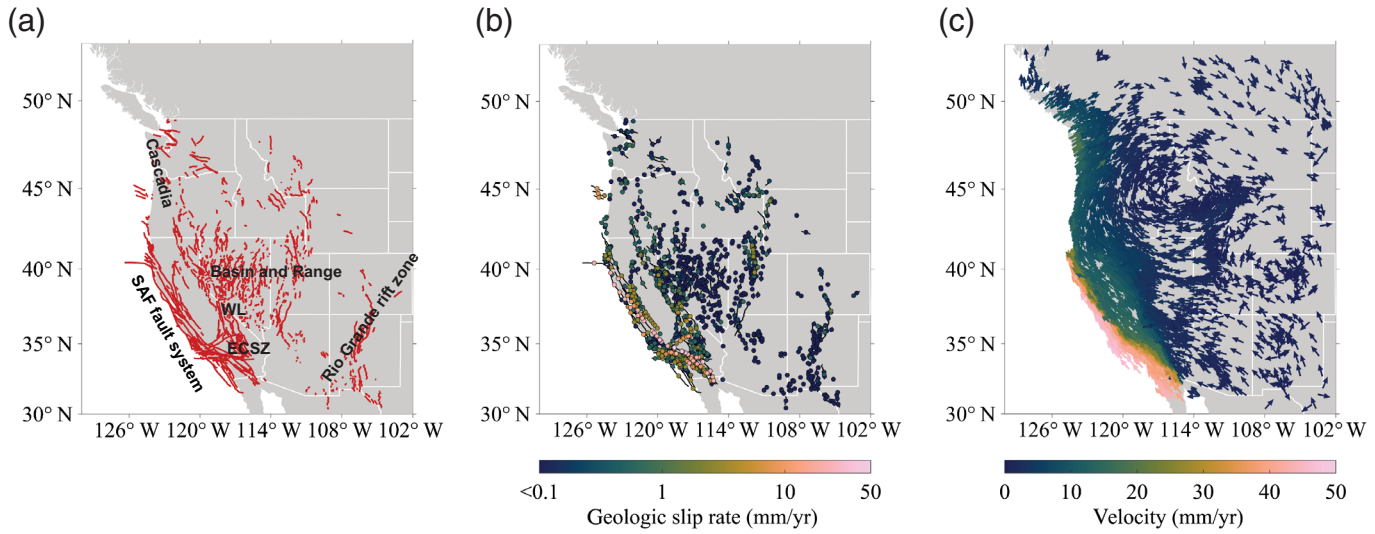

Figure 1. Inputs into the block model. (a) Traces of geologic fault sections from the National Seismic Hazard Mapping (NSHM) Fault Sections database (Hatem, Collett, *et al.*, 2022) in red lines, with major tectonic regions labeled. ECSZ, eastern California shear zone; WL, Walker Lane. (b) Geologic slip rates NSHM Geologic Slip Rates database (Hatem, Collett, *et al.*, 2022) shown at estimate site locations, colored by estimated fault slip rate. (c) Global Navigation Satellite Systems (GNSS) velocity observations from Zeng (2022a). Velocities are shown at a constant length to show relative direction and are colored by velocity magnitude.

deeper in time, but they must average over several earthquake cycles to estimate the fault slip rate (e.g., Sieh and Jahns, 1984; Weldon and Sieh, 1985).

Tectonic geodetic observations are often interpreted within a 3D spherical block model (e.g., McCaffrey, 2005; Meade and Hager, 2005), in which the crust is divided into microplates bounded by faults. GNSS velocities simultaneously constrain the relative rotations of microplates, interseismic elastic deformation due to locked faults, and spatially variable slip deficit rates on meshed fault surfaces (for example, to represent a subduction zone or partially creeping fault, Meade and Loveless, 2009). Fault slip rates are determined by differential rotation rates at block boundaries. However, uncertainty in the appropriate geometry of fault connectivity has limited interpretability of block models, especially at the individual fault level. Furthermore, a high number of closely spaced faults requires either manual choices about which faults are most important or additional regularization of the block model solution.

Total variation regularization (TVR) is an L1 regularization method that regularizes the block model solution by minimizing differences in block rotations on a sphere, resulting in a solution that is quantized. In other words, a dense network of small blocks is algorithmically grouped into fewer, larger blocks based on data constraints. TVR has been applied to block models constrained by GNSS to evaluate fault complexity and distributed deformation in the eastern California shear zone (Evans *et al.*, 2016), to block models jointly constrained by GNSS and geologic slip rates to evaluate fault system complexity in the western continental United States (Evans *et al.*, 2015), and to block models jointly constrained by GNSS and InSAR data (Huang and Evans, 2019).

This work is part of the deformation modeling effort for the 2023 update to the U.S. Geological Survey (USGS) National Seismic Hazard Model (NSHM), along with three other geodetic deformation models (Politz, 2022; Shen, 2022; Zeng, 2022b) and a geologic deformation model (Hatem, Reitman, *et al.*, 2022), all of which will undergo additional review to ensure appropriate incorporation into the NSHM. I model western continental United States (WCUS) tectonic deformation with a block model in which the crust is divided into microplates bounded by the 1017 fault sections included in the NSHM Fault Sections database (NSHM2023 Fault Sections, Hatem, Collett, *et al.*, 2022) and constrained by a combined GNSS velocity field of 4979 velocities (Zeng, 2022a) corrected for interseismic creep (Johnson *et al.*, 2022) and time-dependent earthquake cycle deformation (Hearn, 2022; Fig. 1). The model is additionally constrained by 1243 geologic slip rates (NSHM2023 Slip Rates, Hatem, Collett, *et al.*, 2022; Fig. 1). To effectively construct and constrain a block model that includes all NSHM2023 Fault Sections, I (1) automate a block closure algorithm to automatically generate closed blocks from the NSHM2023 Fault Sections and (2) apply TVR to stabilize the solution. I identify a reference model that fits WCUS GNSS velocities with a root mean square misfit (rms) of 1.9 mm/yr. Formal uncertainties approach infinity on fault bounding blocks with few data constraints, but the TVR produces models with reproducibility of 10–60 mm/yr on most of these unconstrained faults. Off-fault-section (OFS) deformation, defined here as slip on block-bounding faults not included in the NSHM Fault Sections database as a measure of "off-fault" deformation, makes up ≤56% of the total moment rate across the boundary.

Methods

Block model estimation

Block models interpret a geodetically observed velocity field in the context of the relative rotations of discrete microblocks bounded by faults and a first order approximation of earthquake cycle processes (e.g., McCaffrey, 2005; Meade and Hager, 2005). The block modeling methodology was extended to include spatially variable locking on complex fault geometries represented by triangular dislocation elements (TDEs, Meade, 2007) and internal block deformation (e.g., Meade and Loveless, 2009).

In a block model, interseismic velocities ($\mathbf{v}_I$) are represented as a linear combination of block motion ($\mathbf{v}_B$), elastic strain accumulation ($\mathbf{v}_E$) due to locking on block-bounding faults and spatially variable locking on TDEs, and homogeneous elastic strain rate ($\mathbf{v}_{\dot{\epsilon}}$):

$$\mathbf{v}_I = \mathbf{v}_B + \mathbf{v}_E + \mathbf{v}_{\dot{\epsilon}} + \mathbf{v}_R. \tag{1}$$

In equation (1), $\mathbf{v}_R$ are residual velocities due to model error and observational noise. Written in terms of block motions on a sphere, locking rates on TDEs, and homogeneous internal strain rate, the forward problem is

$$\mathbf{v}_I = [\mathbf{G}_B - \mathbf{G}_L, \quad \mathbf{G}_t, \quad \mathbf{G}_{\dot{\epsilon}}] \begin{bmatrix} \boldsymbol{\Omega} \\ \mathbf{t} \\ \dot{\epsilon} \end{bmatrix} + \mathbf{v}_R, \tag{2}$$

in which $\mathbf{G}_B$ contains partial derivatives (Green's functions) of velocity observations with respect to the block motions (Meade and Loveless, 2009), $\mathbf{G}_L$ contains Green's functions associated with locking on surface block-bounding faults (Meade and Loveless, 2009), $\mathbf{G}_t$ contains Green's functions for locking on triangular dislocation elements (Meade, 2007), and $\mathbf{G}_{\dot{\epsilon}}$ contains Green's functions for internal strain rate (Meade and Loveless, 2009); $\boldsymbol{\Omega}$ is the vector of block motions, $\mathbf{t}$ contains the locking rates on TDEs, and $\dot{\epsilon}$ contains the estimated strain rates.

An advantage of block models is that they satisfy the tectonic kinematic consistency constraint (Minster and Jordan, 1978; Humphreys and Weldon, 1994). Kinematic consistency is defined such that a path integral of motion (slip rates and plate rotations) across the plate boundary sums to the total relative tectonic plate motion, independent of path (Minster and Jordan, 1978; Humphreys and Weldon, 1994). In a block model, fault slip rates are linearly proportional to the differential rotation rates at block boundaries (Souter, 1998), so slip rates are implicitly kinematically consistent (Matsu'ura *et al.*, 1986; Bennett *et al.*, 1996; Souter, 1998; McCaffrey, 2002; Meade and Hager, 2005; Meade and Loveless, 2009).

The kinematically consistent slip rate ($\dot{\mathbf{s}}_{obs}$) at the midpoint of a fault segment is proportional to the differential velocity predicted by the relative rotation of the bounding blocks on either side and, therefore, may be isolated in terms of block rotations (Meade and Loveless, 2009):

$$\dot{\mathbf{s}}_{obs} = \mathbf{P}\mathbf{G}_\Delta\boldsymbol{\Omega} + \mathbf{v}_R, \tag{3}$$

in which $\mathbf{P}$ is the geometric projection from differential east and north block motion into fault slip components and $\mathbf{G}_\Delta$ gives the differential velocities at fault segment midpoints due to the relative motion predicted by the rotation of the fault-bounding blocks (Meade and Loveless, 2009). In this way, geologic slip rates are included as supplemental a priori slip rate constraints on individual fault segments (e.g., Meade and Loveless, 2009).

Block closure

Initial block boundaries are defined by the NSHM2023 Fault Sections database (Hatem, Collett, *et al.*, 2022). This database includes 1017 geologically mapped fault sections determined to be potentially relevant for seismic hazard (Fig. 1).

Block models require that model faults connect to form closed blocks. Although faults are likely more connected than their mapped traces suggest (e.g., Page, 2020), block closure often requires that additional model faults be inferred or invented. Because of the high number of densely spaced faults included in the NSHM2023 Fault Sections database, it is impractical to manually connect faults to form closed blocks. To address this, I automate and streamline block closure following an algorithm designed to mimic block closure by inspection, as detailed in the supplemental material available to this article.

Regularization and slip rate estimation

Generating closed blocks from the faults in the NSHM2023 Fault Sections database results in a dense and complex initial block model requiring additional regularization. This is possible due to a novel block modeling approach that algorithmically determines a best-fitting geometry from an initially dense model. TVR is an L1 regularization method developed for edge sharpening in image processing (Rudin *et al.*, 1992; Chambolle, 2004). In an inverse problem, TVR simultaneously minimizes the L2 norm of data residuals and the L1 norm of variation in the state (or solution) vector:

$$\min(\|\mathbf{G}\mathbf{m} - \mathbf{d}\|_2 + \lambda\|\mathbf{D}\mathbf{m}\|_1), \tag{4}$$

in which $\mathbf{G}$ is the generalized Jacobian, $\mathbf{m}$ is the solution vector, $\mathbf{d}$ is the data vector, and $\mathbf{D}$ is a linear differential operator constraining differences in solution vector $\mathbf{m}$ (Evans *et al.*, 2015). Applied to rotation vectors in a block model, TVR minimizes the L1 norm of discrete differences in neighboring block rotations, resulting in a solution with many identical rotation vectors, effectively grouping blocks into fewer, larger blocks and localizing slip on the boundaries of these larger blocks (Evans *et al.*,

2015). Scalar tuning parameter λ controls the degree of grouping. Here, I perform a weighted TVR minimization in which block rotations are jointly constrained by interseismic GNSS velocities ($\mathbf{v}_I$) and geologic slip rates ($\dot{\mathbf{s}}_{obs}$) and in which we simultaneously estimate slip on a mesh of triangular dislocation elements (representing the Cascadia subduction zone) as

$$\min\left(\left\|\mathbf{W}^{\frac{1}{2}}\left(\mathbf{G}\begin{bmatrix}\boldsymbol{\Omega}\\ \mathbf{t}\end{bmatrix}-\begin{bmatrix}\mathbf{v}_I\\ \dot{\mathbf{s}}_{obs}\end{bmatrix}\right)\right\|_2+\lambda\|\mathbf{Dm}\|_1\right), \quad (5)$$

in which $\mathbf{W}$ is a weighting matrix containing GNSS and geologic slip rate covariance matrices and a smoothing constraint for slip on the Cascadia mesh. I apply the regularization only to the block rotations ($\boldsymbol{\Omega}$) and do not estimate the internal block strain. Block adjacency is included in linear operator $\mathbf{D}$, so only neighboring blocks are grouped (Evans *et al.*, 2015).

OFS deformation

I consider most estimated slip on NSHM2023 Fault Sections to be "on-fault" deformation. OFS deformation consists of (1) tensile slip on vertical NSHM2023 Fault Sections (176 of the total 1017 sections) and (2) all slip on faults introduced to satisfy block closure. OFS deformation is collected on a 0.1° by 0.1° geographic grid (e.g., Evans, 2018). To calculate the OFS deformation rate, I sum the moment accumulation rate due to all OFS fault slip rates in each grid cell. The moment in a cell, k, containing N fault segments, is described by equation (6):

$$\dot{\mathrm{Mo}}_k=\mu\sum_{i=1}^{N}\dot{s}_iA_i, \quad (6)$$

in which μ is the shear modulus (assumed here to be 30×10^9 Pa) and $\dot{s}_i$ and A_i are the estimated slip rate and fault area, respectively, of fault segment i in cell k. I assume that the seismogenic depth is no more than 11 km (e.g., appendix E of Petersen *et al.*, 2013).

Input data

The combined GNSS velocity field contains 4979 horizontal velocity vectors (Zeng, 2022a). The GNSS observations were corrected for creep ($\mathbf{v}_{creep}$, Johnson *et al.*, 2022) and for time-dependent earthquake cycle processes ("ghost transients"; v_{GT}, Hearn, 2022). I refer to the velocities corrected only for creep as the "C field" ($\mathbf{v}_C$, equation 7):

$$\mathbf{v}_C=\mathbf{v}_{GNSS}-\mathbf{v}_{creep}. \quad (7)$$

I refer to the velocities corrected for creep and ghost transients as the "CGt field" ($\mathbf{v}_{CGt}$, equation 8):

$$\mathbf{v}_{CGt}=\mathbf{v}_{GNSS}-\mathbf{v}_{creep}-\mathbf{v}_{GT}. \quad (8)$$

The creep and ghost transient corrections allow me to assume that all faults are fully locked to their locking depths and that slip is secular (constant in the interseismic period). These assumptions are built into the block modeling methodology, so I prefer to constrain the model with $\mathbf{v}_{CGt}$ (equation 8).

A total of 1243 geologic slip rates from the NSHM Slip Rates database (Hatem, Collett, *et al.*, 2022) are included as constraints on the model segments spanning each rate location. Preferred geologic rates from Hatem, Collett, *et al.* (2022) (i.e., those based on a published slip rate study) are applied as a priori rates (equation 3). I assume that the a priori rate for binned geologic rates from Hatem, Collett, *et al.* (2022) (i.e. those not based on a published slip rate study) are the mean of the bin boundaries. If multiple rates exist at one location, I apply the average as the a priori rate. Oblique geologic rates are applied as two rates simultaneously: a dip-slip rate and a strike-slip rate, for a total of 1296 a priori rates.

I construct weighting matrix $\mathbf{W}$ that includes provided GNSS and geologic slip rate uncertainties (for simplicity, these are assumed to represent one standard deviation from the mean). Geologic constraints are down weighted relative to GNSS observations by a factor of 10 for a model that is primarily geodetic, as an alternative to the other geodetic deformation models in this Focus Section that weight geologic rates more (Politz, 2022; Shen, 2022; Zeng, 2022b).

I simultaneously estimate slip deficit rate on a mesh of triangular dislocation elements representing the Cascadia subduction zone (equation 2), with the subduction zone geometry determined by McCrory *et al.* 2009. I use the same mesh that is used in Saux *et al.* (2022).

Results

The block closure algorithm produces 853 closed blocks. Manual adjustments to the fault catalog (e.g., removing splays that likely merge at depth) and manual block closure by inspection would likely result in slightly fewer blocks, especially the smallest blocks. However, this is the approximate number of blocks required to connect all of the faults identified in Hatem, Collett, *et al.* (2022) for consistency with other deformation models in this Focus Section (Hatem, Reitman, *et al.*, 2022; Politz, 2022; Shen, 2022; Zeng, 2022b). I consider a suite of 101 λ values (equation 5): 50 values log-distributed from 10 to 10,000 to explore the parameter space and 51 values linearly distributed from 0 to 1000. I apply the TVR with these λ values to the model constrained by the $\mathbf{v}_{CGt}$ velocities, which have been corrected for creep and ghost transients (see the Input data section). Details of model sensitivity to the parameter space (Fig. S3) and results constrained by the $\mathbf{v}_C$ field (corrected for creep only, Figs. S4–S16) are included in the supplemental material.

Reference model and uncertainties

I select a reference model constrained by the $\mathbf{v}_{CGt}$ field at $\lambda=320$, with rms = 1.91 and a total of 351 unique rotation vectors (351 independent blocks; Fig. 2). Residual velocities

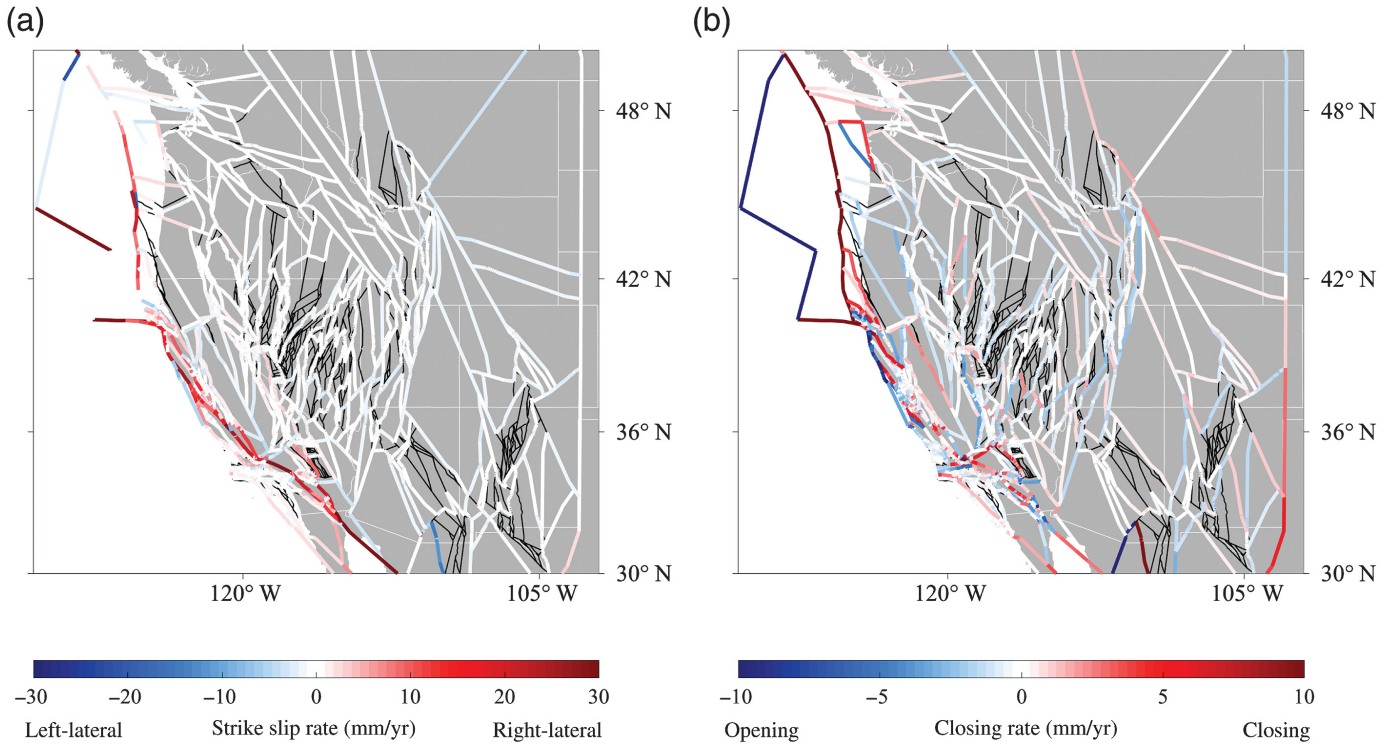

Figure 2. (a) Strike slip rates and (b) dip-slip rates of reference model $\lambda = 320$. Note the different color scale between (a) and (b). Faults with slip rates of exactly zero shown as black lines.

are shown in Figure 3. In models constrained by the $\mathbf{v}_C$, $\lambda = 380$ also results in residual rms = 1.91 (310 blocks), and details of this model are included in the supplemental material (Figs. S4 and S5). This model was selected to fit the GNSS data with an rms misfit of less than 2 mm/yr, and an rms misfit of ~1.9 mm/yr is consistent with the other geodetic deformation models included in this Focus Section (Politz, 2022; Shen, 2022; Zeng, 2022b). I consider two uncertainty metrics on the estimated slip rates. The first is the formally propagated uncertainty in the block model (σ_{formal}; Meade and Loveless, 2009). Many blocks are poorly constrained or unconstrained (280 blocks contain no GNSS observations within them), leading to high uncertainties that approach infinity (up to 1×10^7 mm/yr; Fig. 4a). Northeastern Nevada and the Rio Grande rift zone are particularly poorly constrained: both regions have a high density of mapped faults and a low density of GNSS data.

Alternatively, I note that the selected reference model is just one model among 50 block models with residual rms 1.6–2.5 mm/yr ($\lambda = 20$–1000, Fig. S4). Therefore, I also consider the estimated slip rates from this suite of 50 models to evaluate the sensitivity of slip rates to the λ parameter and use the standard deviation of these slip rates as an alternative uncertainty metric ($\sigma_{\text{sensitivity}}$). The values of $\sigma_{\text{sensitivity}}$ are consistently lower (Fig. 4b). For example, calculated σ_{formal} values are as high as 1×10^7 mm/yr when unconstrained, whereas the highest $\sigma_{\text{sensitivity}}$ value is 56 mm/yr. In addition, in northeastern Nevada and the Rio Grande rift zone, where σ_{formal} is highest, $\sigma_{\text{sensitivity}}$ is relatively low (Fig. 4b). The unconstrained regions are the first to be grouped in the TVR regularization, leading to consistently low slip rates in these regions among the models.

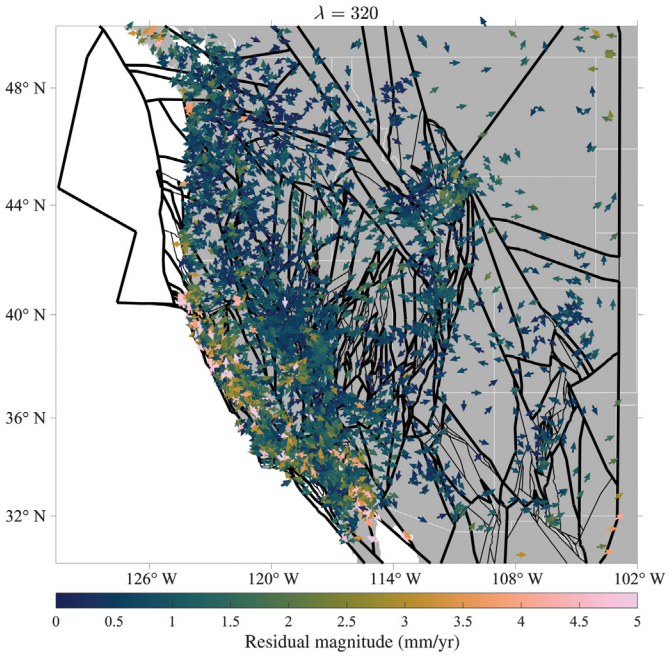

Figure 3. Residual velocities for the reference model $\lambda = 320$. Velocities are shown at a constant length to show the relative direction and are colored by residual velocity magnitude.

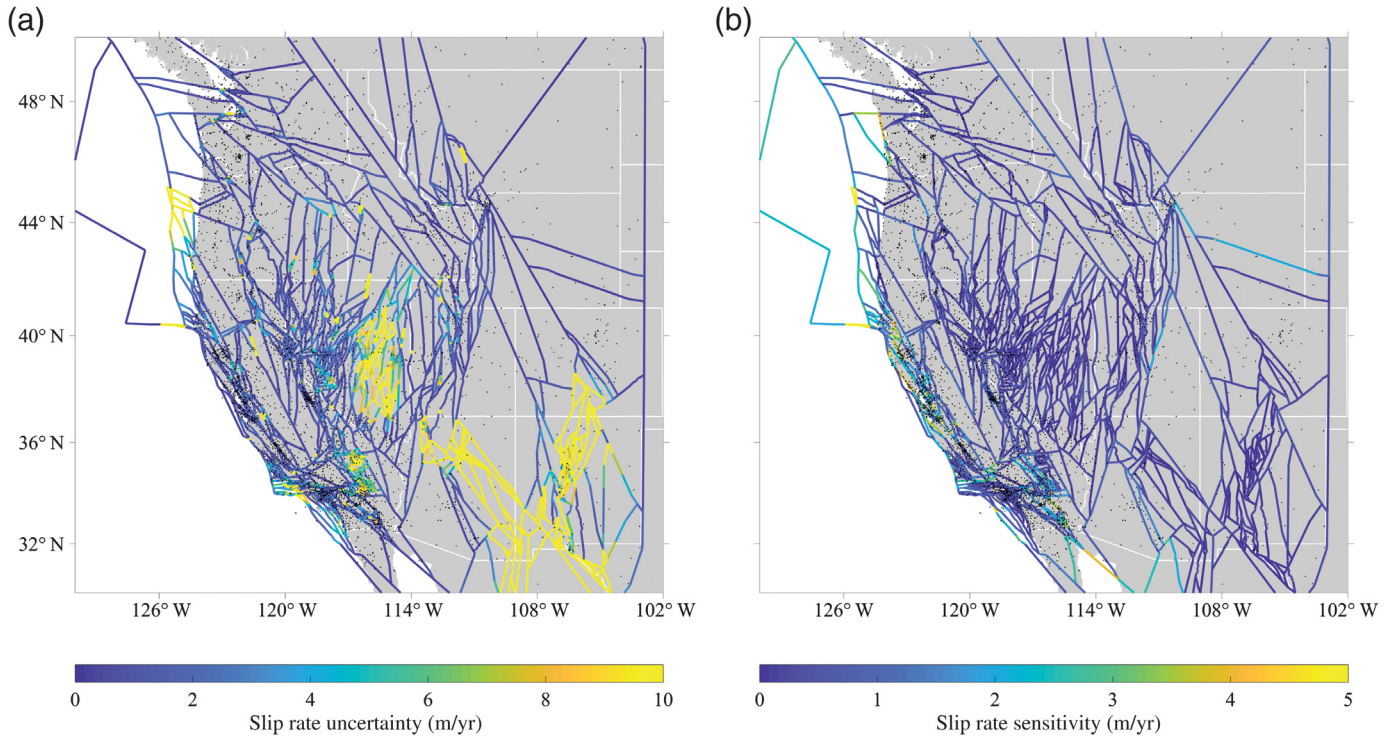

Figure 4. (a) Uncertainties on slip rate estimates calculated as formally propagated uncertainties and (b) model sensitivity. Station locations shown as small black dots. (a) Formally propagated uncertainties approach infinity (up to 1×10^7 mm/yr) on faults bounding unconstrained blocks, especially where GNSS station spacing is sparse. (b) Slip rate sensitivity is the standard deviation of slip rate on a given fault over 50 models with $20 \leq \lambda \leq 1000$. Sensitivity is much lower than the formally calculated uncertainty.

Slip rate ranges described later largely reflect along-fault variability due primarily to changes in fault geometry rather than either formal uncertainty or sensitivity. Faults are identified by name and by the USGS fault identification number (FID).

Southern California

The reference model fits southern California velocities (calculated in the region shown in Fig. 5) with an rms misfit of 2.2 mm/yr. The primary fault in the southern California region is the San Andreas fault (SAF), with right-lateral strike slip rates of 25 ± 1 mm/yr on the Carrizo segment (FID: 707), 17 ± 1 mm/yr in the Big Bend (FID: 706, with up to 18.5 mm/yr contraction), 29 ± 1 mm/yr on the Mojave segment (FID: 704), and 20 ± 3 mm/yr on the Coachella segment (FID: 700). Right-lateral slip from the Coachella segment continues northeast into the ECSZ via the Eureka Creek fault (FID: 79), rather than through the Cajon pass to stay on the SAF. Slip on the Mill Creek segment (FID: 2) between the Mojave and Coachella segments drops to <2 mm/yr strike slip with 4–7 mm/yr reverse slip. Adjacent to this segment, several small faults are active in a complex fault geometry but at low slip rates (<2 mm/yr). The largest slip rate west of the SAF is 21 ± 2 mm/yr on the San Jacinto fault (FID: 21), apparently the southward continuation of most of the deformation from the Mojave segment.

I estimate up to 9.6 mm/yr on the westernmost ~10 km of left-lateral Garlock fault (FID: 880), which decreases to 0–3 mm/yr in the ECSZ (FID: 882 for eastern Garlock); however, the central and eastern Garlock have an estimated closing rate of 5–7 mm/yr. Three through-going strike-slip structures remain active in the ECSZ, including portions of the Lenwood–Lockhart-Old Woman Springs (FID: 142), Gravel Hills–Harper Lake (FID: 89), Camp Rock (FID: 27), Johnson Valley (FID: 129), Blackwater (FID: 17), and Calico-Hidalgo faults (FID: 17), with most slip (6–10 mm/yr) on the Calico-Hidalgo and Blackwater faults.

North of the Garlock fault, 8–11 mm/yr of right lateral slip occurs parallel to the San Andreas fault on the Pleito fault (FID: 215) and an extended Lost Hills fault (on which I also estimate ~3 mm/yr of normal slip, FID: 152) , both of which are geologically considered thrust faults (Hatem, Collett, *et al.*, 2022).

West of the SAF, oblique slip occurs on the San Gabriel fault (FID: 242), Pine Mountain (FID: 208) and Big Pine faults (FID: 16), and the East Huasna fault (FID: 73) at rates of 3–7 mm/yr right lateral and 3–8 mm/yr reverse-slip. The Oceanside fault (FID: 195) converges at 1–3 mm/yr. However, I estimate left-lateral and normal slip on the adjacent Santa Ynez fault (FID 268), suggesting that this region may be poorly constrained geodetically.

Offshore, the San Diego trough (FID: 239) and San Clemente faults (FID: 238) are active at 1 ± 0.5 and 2.5 ± 1 mm/yr, respectively.

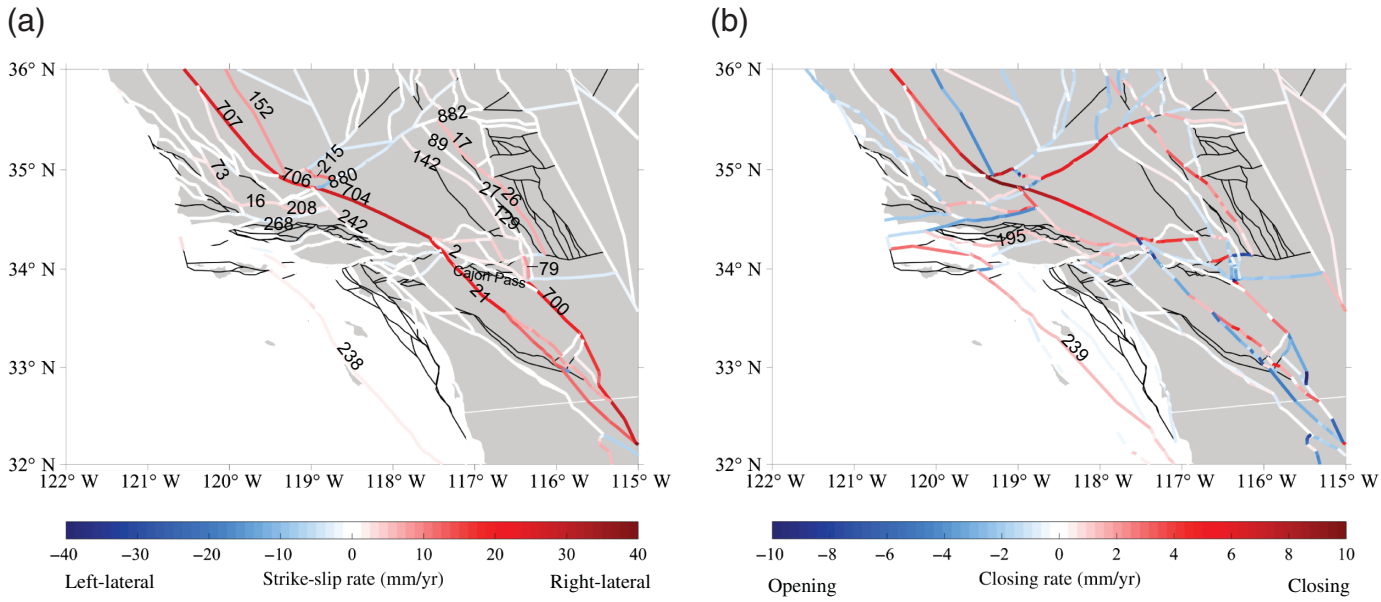

Figure 5. (a) Strike slip rate estimates and (b) opening and closing estimates of the reference model in southern California. Select active faults identified by NSHM Fault section ID number: 2—Mill Creek, 7—Blackwater, 16—Big Pine, 17—Calico–Hidalgo, 21—San Jacinto north, 27—Camp Rock, 79—Eureka Peak, 89—Gravel Hills–Harper Lake, 129—Johnson Valley, 142—Lenwood–Lockhard-Old Woman Springs, 152—Lost hills, 195—Oceanside, 208—Pine mountain, 215—Pleito, 238—San Clemente, 239—San Diego trough, 242—San Gabriel, 268—Santa Ynez, 700—SAF Coachella, 704—SAF Mojave north, 706—SAF Big Bend, 707—SAF Carrizo, 880—Garlock west, and 882—Garlock east.

Northern California

The reference model fits northern California velocities (calculated in the region shown in Fig. 6) with an rms misfit of 2.7 mm/yr. As in southern California, the primary plate boundary in northern California follows the SAF. Moving north from the 33 ± 2 mm/yr central creeping segment (FID: 710) into the San Francisco Bay area, right-lateral slip divides between the 5 and 7 mm/yr Zayante fault (FID: 305), the Peninsula segment of the SAF (FID: 712) at 11 ± 3 mm/yr, the southern Calaveras (10–12 mm/yr, FID: 921), and the Quien Sabe faults (3–4 mm/yr, FID: 223). Slip in the east San Francisco Bay area is concentrated on the Hayward fault (13 ± 1.5 mm/yr, FID: 902). Hayward fault slip continues north primarily on the Maacama fault (FID: 155) at 10 ± 1.5 mm/yr, with only 3 ± 1 mm/yr on the Rodger's Creek fault (FID: 903). The South Napa fault (FID: 354), site of the 2014 West Napa earthquake has an estimated slip rate of ~1 mm/yr. In the northeast part of the fault system, the Bartlett Springs fault (FID: 8) slips at 2–4 mm/yr.

Offshore, the San Gregorio fault (FID: 245) is active at about 8 mm/yr. The westernmost faults in northern California, including the Point Reyes fault (FID: 216) and northernmost offshore portion of the San Andreas fault (FID: 714), accommodate up to 10 mm/yr of opening. A dense, complex network of faults are active near the Mendocino triple junction, including the Russ (4–6 mm/yr right-lateral, up to 18 mm/yr normal slip, FID: 236) and Little Salmon (2–6 mm/yr left-lateral, up to 9 mm/yr thrust slip, FID: 147) faults. Again, this short-wavelength variability suggests that this region may be insufficiently constrained by the GNSS.

Several faults are active in California's Central Valley, at relatively low (<3 mm/yr) slip rates.

Walker Lane and the Basin and Range

The reference model fits Walker Lane and Basin and Range velocities (calculated in the region shown in Fig. 7) with an rms misfit of 1.8 mm/yr. In eastern California and western Nevada, right-lateral strike slip continues up from the eastern California shear zone into the Walker Lane. Although many faults through the Walker Lane remain active, most strike-slip deformation is concentrated on the Paxton Ranch (FID: 331), Owens Valley (FID: 199), and Wassuk Range (FID: 1120) faults at 1–4 mm/yr, continuing onto the Pyramid Lake (FID: 1094) and Warm Springs Valley (FID: 1119) faults. About 60 km to the east, the Ash Hill fault (FID: 6) and Hunter Mountain–Saline Valley fault (FID: 123) are also at 1–3 mm/yr.

The Basin and Range region of the reference model is dominated by low-slip rate (mostly normal or extension) deformation across many subparallel fault systems made up of several interconnected faults. The largest normal slip rates occur on a fault system including the Toiyabe range fault (0.5–2 mm/yr, FID: 1117) between 118° and 116° W, a fault system extending south from the Wasatch fault (FID: 2761) to the Maple Grove (FID: 2762) and Paragonah (FID: 2710) faults (around 113° W, 1–5 mm/yr). The easternmost faults in this system (including Joe's Valley fault, FID: 2709; Hogsback fault, FID: 2921; and Bear river fault, FID: 2900) have the highest normal slip rates of up to 6 mm/yr. We note, however, that this region of the

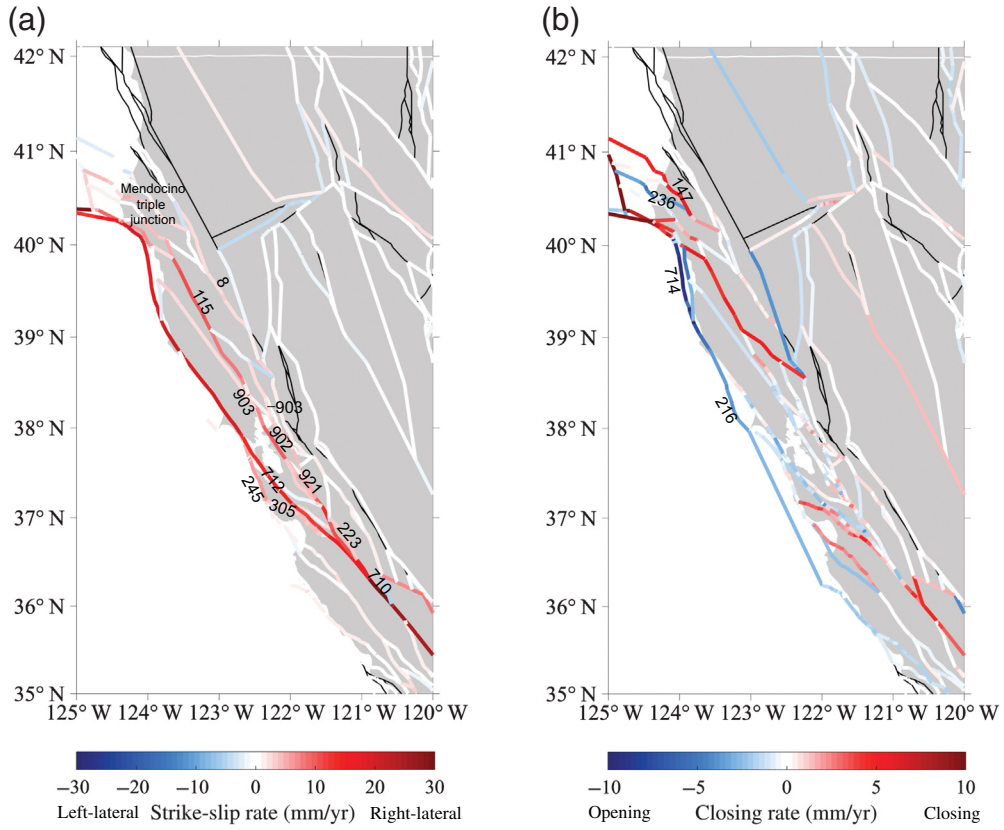

Figure 6. (a) Strike slip rate estimates and (b) opening/closing estimates of the reference model in northern California. Select active faults identified by NSHM Fault section ID number: 8—Bartlett Springs, 147—Little Salmon, 216—San Gregorio north, 223—Quien Sabe, 236—Russ, 245—San Gregorio, 305—Zayante, 354—South Napa, 710—SAF creeping segment, 712—SAF peninsula segment, 714—SAF offshore, 902—Hayward north, 903—Rodgers Creek, and 921—Calaveras south.

model is especially poorly constrained (Fig. 4a), and these rates may be more representative of total regional deformation rather than truly concentrated on the structures described here.

Pacific Northwest

The block model solution includes simultaneous estimation of slip deficit on the Cascadia subduction zone (equation 2). Cascadia slip deficit estimation includes Laplacian smoothing on the mesh of triangular dislocation elements. Details of the estimated slip deficit rates are included in Figure S8. Tradeoffs between modeled megathrust coupling and estimated slip rates on surface faults in the Pacific northwest (e.g., McCaffrey, 2005; Evans *et al.*, 2015) potentially limit interpretation of slip rate results in this region.

In the Pacific northwest, several fault systems remain active (Fig. 8). There is complex activity near the Mendocino triple junction, including the Russ (FID: 236) and Little Salmon (FID: 147) faults discussed in the Northern California section. Farther north and inland, slip rates are primarily right lateral and/or extensional/normal, with the highest slip rates up to 3–4 mm/yr. East of the Mendocino triple junction, Bear Creek fault (FID: 311) is active in northern California, connected to an extension of the Coquille anticline (FID: 2511) and Pioneer (FID: 2569) faults, at rates of up to 1.5 mm/yr right-lateral strike-slip and 2.5 mm/yr normal slip. Two southeast–northwest striking faults, the Alvin Canyon fault (FID: 2504) and Happy Camp fault (FID: 2516), are active onshore and offshore at 1–3 mm/yr. Farther inland, a right-lateral fault system is active around 120° W, including the Albert Rim fault (FID: 2503), southeast Newberry fault (FID: 2533), and Metolius fault (FID: 2522). Additional normal slip of 2–5 mm/yr occurs on the Sky Lakes fault (FID: 2532), Cedar Mountain–Mahogany Mountain fault (FID: 31), and Rocky Ledge fault (FID: 233).

The reference model fits GNSS velocities in Cascadia (calculated in the region shown in Fig. 8) with an rms misfit of 1.4 mm/yr.

OFS deformation

For this study, strike-slip and dip-slip rates on fault sections included in the NSHM2023 Fault Sections database are considered on-fault deformation. All other deformation, including slip on faults added to form closed blocks and opening or closing on vertical faults, is considered "off-fault" deformation or, more precisely, "off-fault-section" (OFS) deformation (Fig. 9). OFS deformation is calculated on a 0.1° by 0.1° grid as described in the OFS deformation section and equation (6).

This results in a total OFS moment accumulation rate of 3.62×10^{19} N · m/yr. This is deformation required to maintain kinematic consistency within this model. For comparison, the total on-fault moment accumulation rate (also assuming a maximum seismogenic depth of 11 km) is 2.84×10^{19} N · m/yr. In other words, 56% of the total deformation accommodated for in this model is accommodated for in the NSHM2023 Fault Sections. Assuming that this deformation is entirely due to locked faults through the seismogenic depth and, therefore, fully seismogenic, this OFS deformation is equivalent to one M_w 6.9 earthquake a year, or one M_w 8.3 earthquake every 100 yr.

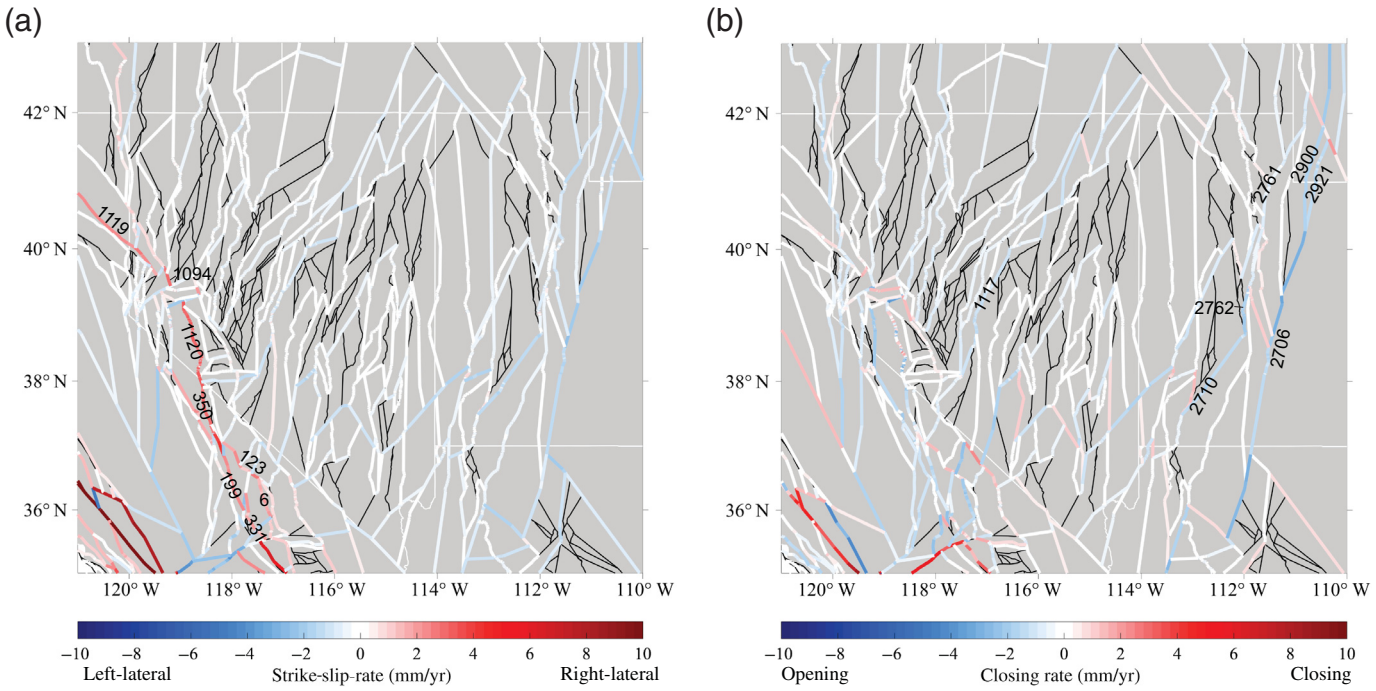

Figure 7. (a) Strike slip rate estimates and (b) opening/closing estimates of the reference model in Walker Lane and the Basin and Range. Select active faults identified by NSHM Fault section ID number: 6—Ash Hill, 123—Hunter Mountain–Saline Valley, 199—Owens Valley, 331—Paxton Ranch, 1094—Pyramid Lake, 1117—Toiyabe, 1119—Warm Springs Valley, 1120—Wassuk Range, 2709—Joe's Valley, 2710—Paragonah, 2761—Wasatch, 2762—Maple Grove, 2900—Bear River, and 2921—Hogsback.

However, I note that with this methodology I am unable to distinguish between distributed seismogenic moment accumulation rates and aseismic off-fault deformation. Furthermore, short-wavelength variability in poorly constrained regions (e.g., near the Santa Ynez fault in southern California and the Russ and Little Salmon faults in northern California) likely falsely inflates both on- and off-fault moment rates. In other words, the OFS moment accumulation rate presented here likely represents an upper bound for seismic hazard.

Discussion

Although the slip rates presented here represent the most complete block-model-based estimates of WCUS to date, they are dependent on both the initial fault geometry and the TVR regularization. Furthermore, all rates should be considered in the context of the high formal uncertainties described in the Reference model and uncertainties section. Regions dominated by poorly constrained blocks and high formal uncertainties, in particular eastern Nevada and the Rio Grande rift, indicate regions in which GNSS data are insufficient to constrain fault-based deformation at the resolution of the faults included in the NSHM2023 Fault Sections database. To capture contemporary WCUS deformation and resolve fault slip on the density of faults included here, these regions may be high priorities for additional GNSS coverage, despite low deformation rates.

Geologic slip rates

Geologic slip rates are included as constraints in the block model solution, although the geologic point data are downweighted relative to the GNSS data. Of the 1296 geologic slip rates applied as a priori rates (oblique slip rates are applied as separate dip-slip and strike-slip rates, see the Input data section), 737 (57%) agree with the geodetic estimate within geologic uncertainty and model sensitivity (see the Reference model and uncertainties section). Of these, 172 of 326 strike-slip rates agree (52%) and 565 of 970 dip-slip rates agree (58%), so there does not appear to be a significant difference in the model's ability to reproduce a particular style of slip. Of the slip rates that do not agree, 342 are lower than the geologic slip rate, and 217 are higher. This behavior may be expected among the poorly constrained "binned" rates (as defined by Hatem, Collett, *et al.*, 2022) for which true geologic rates may be at the low end of the bin. However, geologic slip rates are more likely to be higher than the geodetic slip rates among the "preferred" geologic rates (Hatem, Collett, *et al.*, 2022): the geodetic rate is lower than 41% of the preferred geologic rates (57% preferred rates agree), and the geodetic rate is lower than only 22% of the binned rates (62% binned rates agree). The difference in agreement between preferred and binned rates (binned rates are more likely to agree) may simply reflect the larger uncertainty ranges associated with the binned rates and may suggest that uncertainties in preferred rates are unrealistically low.

Some slip rate comparisons between the geologic data and the geodetic reference model are highlighted in Figure 10.

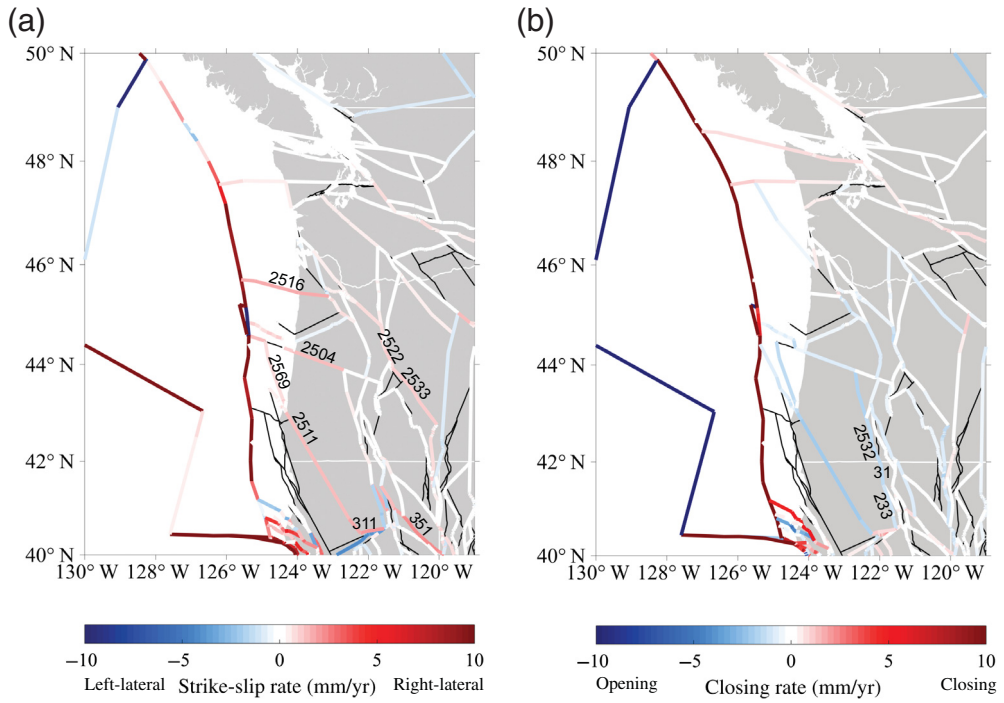

Figure 8. (a) Strike slip rate estimates and (b) opening/closing estimates of the reference model in the Pacific northwest. Select active faults identified by NSHM Fault section ID number: 31—Cedar mountain–Mohogany mountain fault, 233—Rocky Ledge, 311—Bear Creek, 351—Susanville–Eagle Lake (unnamed proxy), 2503—Albert Rim, 2504—Alvin Canyon, 2511—Coquille Anticline, 2516—Happy Camp, 2522—Metolius, 2532—Sky Lakes, 2533—southeast Newberry, and 2569—Pioneer.

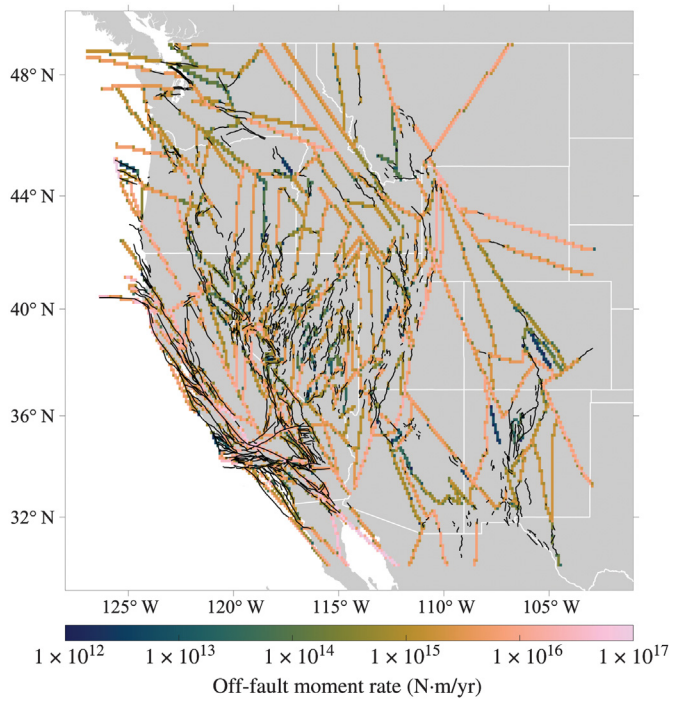

Figure 9. Off-fault section (OFS) moment rate includes slip on faults added to form closed blocks and opening/closing on vertical faults. Assumed shear modulus is 30 GPa.

Vertical geodetic error bars are defined by the slip rate sensitivity ($\sigma_{sensitivity}$) described in the Reference model and uncertainties section). Horizontal geologic error bars define the edges of bins defined in the NSHM2023 Slip Rates database. For geologic rates without a preferred rate, the comparison rate is taken to be the average of the bin boundaries. At high slip rates, a discrepancy occurs on the Mendocino fault, with a geodetic slip rate of 40 ± 6.8 mm/yr and a binned geologic rate between 5 and 35 mm/yr, and on the Mojave segment of the SAF, with a geodetic rate of 28 ± 1.6 and a binned geologic rate between 34 and 51 mm/yr. Several other SAF geodetic rates are lower than the geologic rate: the San Bernardino segment has geologic rates of 19–31 mm/yr and a geodetic estimate of 2 ± 1.25 mm/yr. The San Bernardino and Coyote Creek segments of the San Jacinto fault have higher geodetic estimates than geologic rates (21.2 ± 2.1 and 13.0 ± 1.6 mm/yr geodetically vs. 3.3 + 31.7/−1.6 and 5.7–8.9 mm/yr geologically, respectively). The Calico and Blackwater faults in the ECSZ also have higher geodetic estimates than geologic rates (7.7 ± 2.6 and 6.5 ± 1.9 mm/yr geodetically vs. 1.4 ± 0.4 and 0.49 ± 0.4 mm/yr geologically, respectively).

Many dip-slip rates are quite low (<5 mm/yr), but the geodetic estimates and geologic rates are not necessarily consistent (Fig. 10b). For example, the Noyo Basin fault, the Russ fault, and the Mission ridge faults have very low (≤1 mm/yr) geologic rates but higher geodetic rates (19.8 ± 0.9 mm/yr, 13.3 ± 2.0 mm/yr, and 7.7 ± 1.5 mm/yr, respectively). Conversely, the San Cayetano and Santa Susana faults have relatively high geologic rates (5–13 mm/yr and 5–35 mm/yr, respectively), but the geodetic estimate is zero.

Geographically, the patterns of discrepancies are consistent with discrepancies identified in previous work (e.g., Evans, 2018; Fig. 11). Geodetic slip rates are consistently lower than geologic rates on the San Andreas fault system, especially on the Carrizo and Mojave segments. Right-lateral geodetic slip rates are higher than geologic rates in the eastern California shear zone, in particular on the Calico and Blackwater faults, whereas the geodetic slip rate on the Garlock fault is lower. These

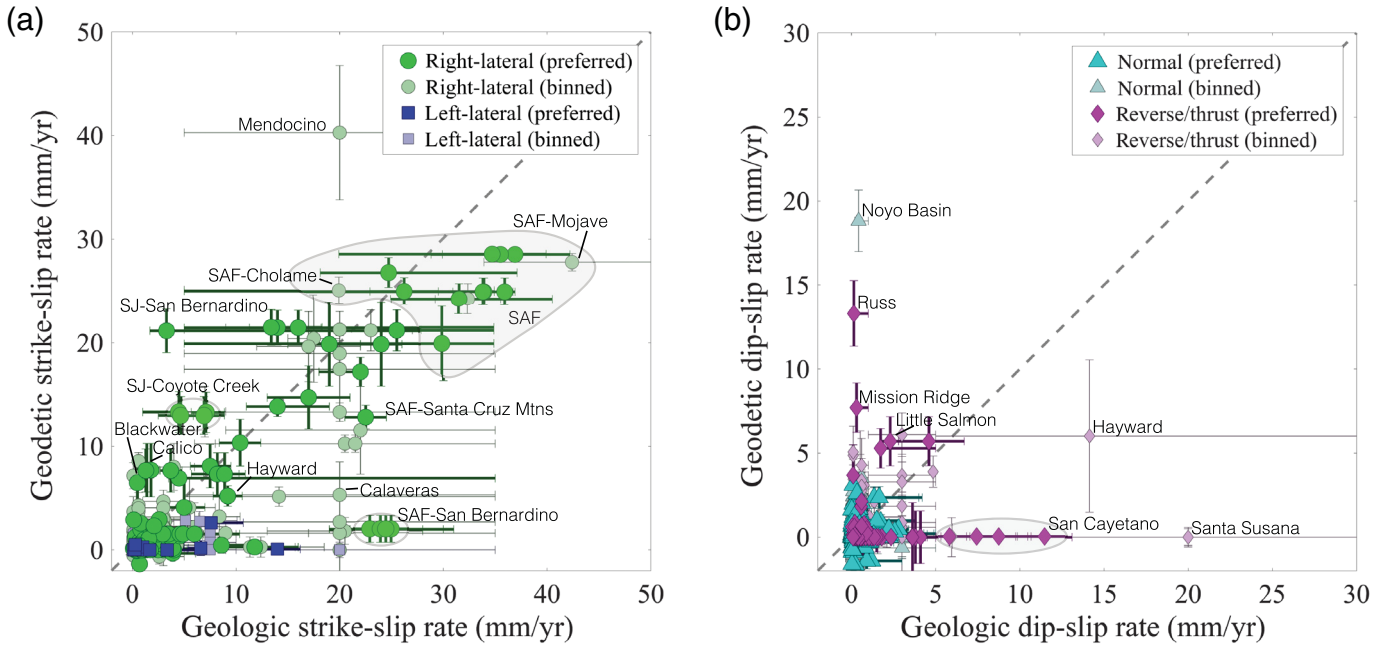

Figure 10. Comparison of geologic slip rates and geodetic slip rates from the reference model. Horizontal error bars indicate geologic uncertainty or bin bounds. Vertical error bars indicate slip rate sensitivity (see the Southern California section). (a) Strike-slip rate comparison with select faults identified. Shaded areas indicate several rates on the same fault or fault section and (b) dip-slip rate comparison with select faults identified.

discrepancies are consistent with previous geodetic models in this region (e.g., Peltzer *et al.*, 2001; Spinler *et al.*, 2010; Chuang and Johnson, 2011; McGill *et al.*, 2015, Evans *et al.*, 2016); the Calico-Hidalgo and Blackwater rates (6–7 mm/yr) are lower than in some geodetic studies but still significantly higher than the <2 mm/yr geologic rates. Geologic rates are consistently higher than geodetic rates in the Basin and Range, although slightly lower in Walker Lane and on the Wasatch fault.

The ghost transient correction

Because the block model formulation assumes secular interseismic velocities, I have presented results based on the $\mathbf{v}_{CGt}$ velocity field, which has been corrected for time-dependent earthquake cycle behavior (the "ghost transient", Hearn, 2022) in addition to a correction for interseismic creep (Johnson *et al.*, 2022; see the Input data section). The supplemental material contains companion figures for a comparable model constrained by the $\mathbf{v}_C$ velocities (corrected only for interseismic creep). Both models fit the input velocity field with an rms of 1.9 mm/yr, although the $\mathbf{v}_C$ model residuals are slightly smaller than the $\mathbf{v}_{CGt}$ model residuals along the SAF but generally larger elsewhere (Fig. S17). The primary difference between the modeled slip rates is that the $\mathbf{v}_{CGt}$ model has faster slip rates along the San Andreas fault by up to 10 mm/yr on the Mojave segment (Fig. 12). In other words, the non-ghost-transient corrected model results in slip rates with greater discrepancies with geologic rates on the San Andreas fault.

Conclusions

I present a block model of WCUS deformation consisting of 853 blocks bounded by 1017 fault sections and constrained primarily by 4979 GNSS velocities and weakly constrained by 1243 geologic slip rates. The block model solution is regularized with TVR to identify the most important block

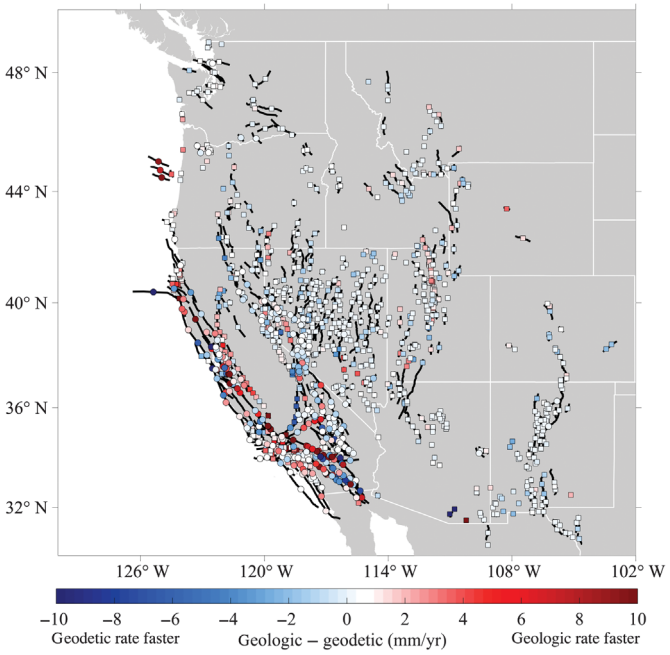

Figure 11. Geographic distribution of geologic versus geodetic slip rates from the reference model.

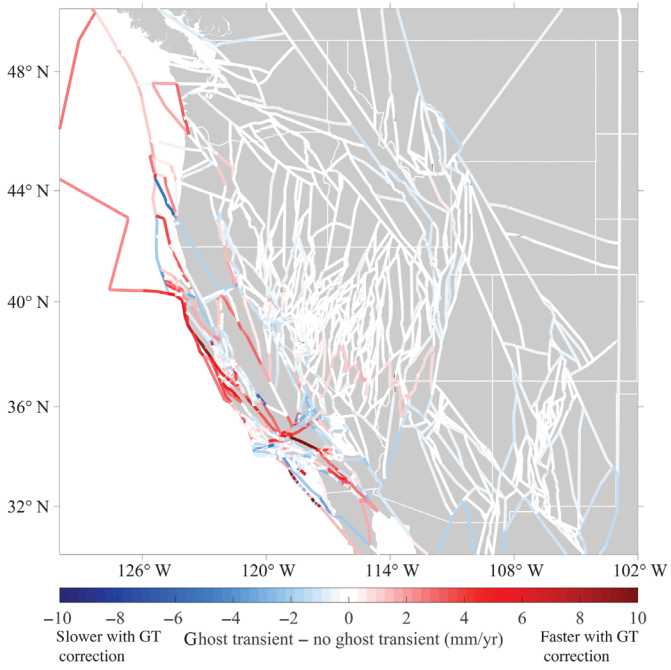

Figure 12. Difference between comparable block models constrained by the $\mathbf{v}_{CGt}$ velocity field, which contains a ghost-transient correction, and the $\mathbf{v}_{C}$ velocity field, which does not. Velocities are shown at a constant length to show the relative direction and are colored by velocity magnitude.

boundaries as required by the geologic and geodetic data. Many blocks are poorly constrained, leading to a broad range of possible slip rates and high uncertainties, highlighting regions that require more GNSS coverage to constrain geodetic deformation for seismic hazard. The regularized solution fits the GNSS velocity field with an rms of 1.9 mm/yr and reproduces 57% of geologic slip rates within reported geologic uncertainty and model sensitivity. I estimate that off-fault deformation makes up ≤56% of the total moment accumulation rate in the WCUS. This work represents the most complete and geologically accurate block model of the WCUS created to date.

Data and Resources

The supplemental material to this article contains additional details regarding block closure, regularization parameter selection, subduction zone slip, and block model results constrained by Global Navigation Satellite System (GNSS) velocities that are not corrected with a ghost transient. All data used in this article came from published sources listed in the references. Model inputs and results in the blocks format are included as supplemental material. Results in the form of tabulations of on-fault and off-fault rates will be made available through U.S. Geological Survey (USGS) ScienceBase (https://www.sciencebase.gov/catalog/item/62bf3457d34e82c548ced92a, last accessed August 2022).

Declaration of Competing Interests

The author acknowledges that there are no conflicts of interest recorded.

Acknowlegments

This work was funded by the U.S. Geological Survey (USGS) IPA 4500145364, National Science Foundation (NSF) EAR-Tectonics Award Number 2141593 and by California State University, Northridge. The author thanks Richard Styron and an anonymous reviewer for thoughtful and thorough reviews that greatly improved the quality of this article and Fred Pollitz, Alexandra Hatem, Johanna Nevitt, Ned Field, Mark Petersen, Yuehua Zeng, and Zheng-Kang Shen for productive conversations while developing this model. Figures were generated in MATLAB, including maps created with the M_Map package (Pawlowicz, R., 2020, available online at https://www.eoas.ubc.ca/~rich/map.html). Colormap batlow used in Figures 1, 3, and 10 was created by Fabio Cramer (http://www.fabiocrameri.ch/batlow.php). All websites were last accessed in August 2022.

References

Bennett, R. A., W. Rodi, and R. E. Reilinger (1996). Global positioning system constraints on fault slip rates in southern California and northern Baja, Mexico, *J. Geophys. Res.* **101,** 21,943–21,960.

Chambolle, A. (2004). An algorithm for total variation minimization and applications, *J. Math. Imag. Vis.* **20,** 89–97.

Chuang, R.Y., and K.M. Johnson (2011). Reconciling geologic and geodetic model fault slip-rate discrepancies in southern California: Consideration of nonsteady mantle flow and lower crustal fault creep, *Geology* **39,** 627–630 doi: 10.1130/G32120.1.

Evans, E. L. (2018). A comprehensive analysis of geodetic slip-rate estimates and uncertainties in California, *Bull. Seismol. Soc. Am.* **108,** no. 1, 1–18.

Evans, E. L., J. P. Loveless, and B. J. Meade (2015). Total variation regularization of geodetically and geologically constrained block models for the western United States, *Geophys. J. Int.* **202**, 713–727.

Evans, E. L., W. R. Thatcher, F. F. Pollitz, and J. R. Murray (2016). Persistent slip rate discrepancies in the eastern California (USA) shear zone, *Geology* **44**, 691–694.

Hatem, A. E., C. M. Collett, R. W. Briggs, R. D. Gold, S. J. Angster, P. M. Powers, E. H. Field, M. Anderson, Y. J. Ben-Horin, T. Dawson, *et al.* (2022). Earthquake geology inputs for the US National Seismic Hazard Model (NSHM) 2023 (western US) (ver. 2.0, February 2022), *U.S. Geol. Surv. Data Release*, doi: 10.5066/P9AU713N.

Hatem, A. E., N. G. Reitman, R. W. Briggs, R. D. Gold, J. A. Thompson Jobe, and R. Burgette (2022). Western U.S. geologic deformation model for use in the U.S. National Seismic Hazard model 2023, *Seismol. Res. Lett.* doi: 10.1785/0220220154.

Hearn, E. (2022). "Ghost transient" corrections to the southern California GPS velocity field from San Andreas fault seismic cycle models, *Seismol. Res. Lett.* doi: 10.1785/0220220156.

Huang, M., and E. L. Evans (2019). Total variation regularization of geodetically constrained block models in southwest Taiwan, *J. Geophys. Res.* **124,** 13,269–13,285.

Humphreys, E. D., and R. J. Weldon (1994). Deformation across the western United States: A local estimate of Pacific-North America transform deformation, *J. Geophys. Res.* **99,** 19,975–20,010.

Johnson, K. M., C. Wespestad, and J. R. Murray (2022). Creep rate data and models for the 2023 update to the US National Seismic Hazard Model, *Seismol. Res. Lett.*

Matsu'ura, M., D. D. Jackson, and A. Cheng (1986). Dislocation model for aseismic crustal deformation at Hollister, California, *J. Geophys. Res.* **91,** 2661–2674.

McCaffrey, R. (2002). Crustal block rotations and plate coupling, *Geodynamics* **30,** 101–122.

McCaffrey, R. (2005). Block kinematics of the Pacific-North America plate boundary in the southwestern United States from inversion of GPS, seismological, and geologic data, *J. Geophys. Res.* **110,** 1978–2012.

McCrory, P. A., J. L. Blair, D. H. Oppenheimer, and S. R. Walter (2009). Depth to the Juan de Fuca slab beneath the Cascadia subduction margin—a 3-D model sorting earthquakes, *U.S. Geological Survey Data Series 91*, version 1.2.

McGill, S. F., J. C. Spinler, J. D. McGill, R. A. Bennett, M. A. Floyd, J. E. Fryxell, and G. J. Funning (2015). Kinematic modeling of fault slip rates using new geodetic velocities from a transect across the Pacific–North America plate boundary through the San Bernardino mountains, California, *J. Geophys. Res.* **120,** 2772–2793.

Meade, B. J. (2007). Algorithms for the calculation of exact displacements, strains, and stresses for triangular dislocation elements in a uniform elastic half space, *Comput. Geosci.* **33,** 1064–1075.

Meade, B. J., and B. H. Hager (2005). Block models of crustal motion in southern California constrained by GPS measurements, *J. Geophys. Res.* **110,** no. B3, doi: 10.1029/2004JB003209.

Meade, B. J., and J. P. Loveless (2009). Block modeling with connected fault-network geometries and a linear elastic coupling estimator in spherical coordinates, *Bull. Seismol. Soc. Am.* **99,** 3124–3139.

Minster, J. B., and T. H. Jordan (1978). Present-day plate motions, *J. Geophys. Res.* **83,** 5331–5354.

Page, M. T. (2020). More fault connectivity is needed in seismic hazard analysis, *Bull. Seismol. Soc. Am.* **111,** 391–397.

Peltzer, G., F. Crampé, S. Hensley, and P. Rosen (2001). Transient strain accumulation and fault interaction in the eastern California shear zone, *Geology* **29,** no. 11, 975–978.

Petersen, M. D., M. P. Moschetti, P. M. Powers, C. S. Mueller, K. M. Haller, A. D. Frankel, Y. Zeng, S. Rezaeian, S. C. Harmsen, O. S. Boyd, *et al.* (2014). Documentation for the 2014 update of the United States National Seismic Hazard maps, *U.S. Geol Surv. Open-File Rept.* doi: 10.3133/ofr20141091.

Petersen, M. D., Y. Zeng, K. M. Haller, R. McCarey, W. C. Hammond, P. Bird, M. Moschetti, Z.-K. Shen, J. Bormann, and W. Thatcher (2013). Geodesy-and geology-based slip-rate models for the Western United States National Seismic Hazard maps, *USGS Open-File Rept.*, 2013–1293.

Politz, F. F. (2022).Viscoelastic fault-based model of crustal deformation for the 2023 update to the U.S. National Seismic Hazard Model, *Seismol. Res. Lett.* doi: 10.1785/0220220137

Rudin, L. I., S. Osher, and E. Fatemi (1992). Nonlinear total variation based noise removal algorithms, *Phys. D Nonlinear Phenom.* **60,** 259–268.

Saux, J. P., E. G. M. Bergman, E. L. Evans, and J. P. Loveless (2022). The role of slow slip events in the Cascadia subduction zone earthquake cycle, *J. Geophys. Res.* **127,** e2021JB022425.

Savage, J. C., and R. O. Burford (1973). Geodetic determination of relative plate motion in central California, *J. Geophys. Res.* **78,** 832–845.

Shen, Z.-K. (2022). Neokinema deformation model for the 2023 update to the US National Seismic Hazard Model, *Seismol. Res. Lett.*

Sieh, K. E., and R. H. Jahns (1984).Holocene activity of the San Andreas fault at Wallace creek, California, *GSA Bull.* **95,** no. 8, 883–896.

Souter, B. J. (1998). Comparisons of geologic models to GPS observations in southern California, *Ph.D. Thesis*, Massachusetts Institute of Technology, Cambridge, Massachusetts.

Spinler, J. C., R. A. Bennett, M. L. Anderson, S. F. McGill, S. Hreinsdóttir, and A. McCallister, (2010). Present-day strain accumulation and slip rates associated with southern San Andreas and eastern California shear zone faults, *J. Geophys. Res.* **115,** no. B11, doi: 10.1029/2010JB007424.

Thatcher, W., J. C. Savage, and R. W. Simpson (2016). The eastern California shear zone as the northward extension of the southern San Andreas fault, *J. Geophys. Res.* **121,** 2904–2914.

Wallace, R. E., and W. R. Dickinson (1968). Notes on stream channels offset by the San Andreas fault, southern Coast Ranges, California, *Conference on Geologic Problems of the San Andreas Fault System. Stanford University Publication in Geological Sciences*, Vol. 11.

Weldon, R. J., and K. E. Sieh (1985). Holocene rate of slip and tentative recurrence interval for large earthquakes on the San Andreas fault, Cajon Pass, southern California, *GSA Bull.* **96,** 793–812.

Zeng, Y. (2022a). Interseismic velocity field of the western U.S. from GNSS, *Seismol. Res. Lett.*

Zeng, Y. (2022b). Deep-slip driven fault-based deformation model for the 2023 update to the US National Seismic Hazard Model, *Seismol. Res. Lett.*

Manuscript received 2 May 2022
Published online 31 August 2022